

MORPHOLOGICAL PROPERTIES OF THE CRAB NEBULA: A DETAILED
MULTIWAVELENGTH STUDY BASED ON NEW VLA, *HST*, *CHANDRA* AND
XMM-NEWTON IMAGES.

G. DUBNER^{1,2} AND G. CASTELLETTI^{1,2}

—

O. KARGALTSEV³

—

G. G. PAVLOV⁴

—

M. BIETENHOLZ^{5,6}

—

A. TALAVERA⁷

¹*Universidad de Buenos Aires. Facultad de Cs. Exactas y Naturales. Buenos Aires, Argentina*

²*CONICET-Universidad de Buenos Aires. Instituto de Astronomía y Física del Espacio (IAFE)
CC 67, Suc. 28, 1428 Buenos Aires, Argentina*

³*Department of Physics, George Washington University
Washington DC 20052, USA*

⁴*Department of Astronomy and Astrophysics
Pennsylvania State University, University Park, PA 16802, USA*

⁵*Hartebeesthoek Radio Astronomy Observatory
P.O. Box 443, Krugersdorp 1740, South Africa*

⁶*Department of Physics and Astronomy, York University
Toronto, M3J 1P3 Ontario, Canada*

⁷*XMM-Newton Science Operations Centre, ESA
Villafranca del Castillo, Apartado 78, E-28691, Villanueva de la Cañada, Spain*

Submitted to ApJ

ABSTRACT

We present a detailed analysis of the morphological properties of the Crab Nebula across the electromagnetic spectrum based on new and previous high-quality data from radio to X-rays. In the radio range we obtained an image of the entire nebula at 3 GHz with subarcsecond angular resolution using the VLA (NRAO) and an image at 100 GHz of the central region using the ALMA array. Simultaneously with the VLA observations we performed *HST* WFPC3 near infrared ($\lambda \sim 1.5\mu\text{m}$) and *Chandra* X-ray (0.5–8 keV band) observations of the central region of the nebula. In addition we produced a new UV image of the Crab nebula at 291 nm by co-adding 75 individual exposures of the Optical-UV Monitor on board *XMM-Newton*. The high-angular resolution and high-dynamic range radio image at 3 GHz allowed us to improve the detection and characterization of peculiar morphological features including arches with foot brightening and intercrossed loop-like structures, likely originating in plasma confined to magnetic field lines. Based on the new radio image, we carried out a detailed multiwavelength correlation. In the central area, the comparison of the almost simultaneous images confirms that the wisps in the three spectral ranges do not generally coincide in location, the radio emission being the most discordant, which is suggestive of the existence of two different synchrotron components. The X-ray pulsar jet does not have a radio counterpart. Instead, another jet-like feature is seen in radio, though with different curvature and starting point.

Keywords: ISM: supernova remnants — ISM: individual: Crab Nebula — radio continuum: ISM — Ultraviolet: ISM — X-rays: ISM

1. INTRODUCTION

The Crab Nebula is the archetype of the nebula created through the interaction of the ultrarelativistic wind injected by a rapidly rotating neutron star, the so-called pulsar wind nebula (PWN). As a very bright object located at a distance of 2 kpc ([Trimble 1973](#)), it is an advantageous target to investigate physical processes in PWNe as well as in supernova remnants (SNRs). Thousands of articles have been published reporting multiwavelength observations and theoretical models describing and interpreting the Crab Nebula. Yet, in spite of being one of the best studied objects beyond our own solar system, there is still much to learn about it.

The wealth of existing data from low radio frequencies to very high-energy gamma rays reveals a very rich and dynamic structure created by the pulsar wind expanding through the remainings of a stellar explosion. The reviews by [Hester \(2008\)](#) and [Bühler & Blandford \(2014\)](#) provide extensive overviews of the current knowledge on this source. In a simplified picture, there are three different components from inside out: (i) the 33 millisecond pulsar PSR B0531+21 (J0534+2200) powering the nebula, (ii) the synchrotron-emitting shocked pulsar's wind, highly dynamic and with a wealth of fine-scale structure, and (iii) a network of thermal filaments from the ejecta (and possibly some material from the precursor stellar wind) compressed by the PWN. A fourth component would be a much larger, almost unseen, freely expanding SNR, claimed to have been detected in the UV by means of C IV $\lambda 1550$ absorption ([Sollerman et al. 2000](#)). However, the outer shock of the expanding SNR has not yet been detected despite considerable searching efforts. In what follows we summarize the main observational characteristics of the Crab Nebula in different spectral ranges between radio and X-rays.

The synchrotron nebula expands within the “cage” of filaments beautifully displayed in emission lines in visible light (e.g. [Hester et al. 1995, 1996](#); [Sankrit & Hester 1997](#); [Loll et al. 2013](#)). Most of the emission from the filaments is the result of photoionization by the hard continuum from the synchrotron PWN emission; there is also emission arising from radiative cooling behind the shock driven by the PWN into the freely expanding ejecta ([Sankrit et al. 1998](#)). The edge of the synchrotron nebula moving outward faster than the local expansion velocity has swept up what is called the “skin,”

a thin shell of thermal material that apparently marks the local boundary of the synchrotron nebula. The center of the nebula is characterized by a torus that surrounds the pulsar in the equatorial plane of the neutron star and a jet aligned with the spin axis of the pulsar. These features are highly dynamic. The most prominent features in the torus move outward with speeds of up to $\sim 0.5c$ as observed in optical, infrared, and in X-rays (Hester 2008, and references therein). Some synchrotron features in the torus, called wisps,¹ are also seen in radio, but, as described below, they do not match up well with the wisps seen in visible light and in X-rays.

In the infrared (IR) domain several observations of the Crab Nebula have been conducted both from Earth in the near-IR (e.g. Sollerman 2003; Tziamtzis et al. 2009) and from space in mid- and far- IR using *IRAS* (Marsden et al. 1984), *ISO* (Douvion et al. 2001; Green et al. 2004), *Spitzer* (Temim et al. 2006, 2012), and *Herschel* (Gomez et al. 2012). Persi (2012) presents a review of previous IR studies. The emission of the Crab Nebula in the near- and mid-IR is dominated by continuum synchrotron radiation, while the emission observed in the far-IR (24 and 70 μm *Spitzer* images) may be due to line emission or to the presence of a small amount of warm dust (Temim et al. 2006). In the FIR domain, the Crab Nebula has also been explored using PACS (wavelengths from 70 to 160 μm) and SPIRE (from 250 to 500 μm) on board of *Herschel*. Based on these observations, Gomez et al. (2012) reported the existence of a cool dust component along the ionized filamentary structure, spatially coincident with the location of ejecta material.

In the X-ray range, the Crab Nebula was one of the first discovered extrasolar sources, when in the early stages of the X-ray astronomy it was detected with a rocket-borne experiment (Gursky et al. 1963; Bowyer et al. 1964). Over the years the pulsar and the nebula have been observed using almost all available instruments (see e.g. Weisskopf et al. 2000; Mori et al. 2004; Seward et al. 2006; Madsen et al. 2015, and references therein). The X-ray remnant is smaller than the optical and IR nebula, which is reasonably explained by the fact that the X-ray emitting electrons have a shorter lifetime than the lower energy electrons emitting optical and IR radiation. In the 1-10 keV band only $\sim 5\%$

¹ By convention the optical features seen in the synchrotron nebula are called “wisps” (other identified features are “sprite” and “knots”), while the thermal gas structures seen in emission lines are called “filaments” (Hester 2008).

of the radiation comes from the pulsar, while most of the nebular X-ray emission originates in the equatorial torus and jet (Brinkmann et al. 1985; Hester et al. 1995). Seward et al. (2006) reported *Chandra* observations revealing for the first time the existence of faint structures forming fingers, loops, and bays in all directions beyond the bright torus-jet structure, whose spectra soften with the distance from the pulsar. The authors suggest that the structure is determined by the synchrotron lifetime of diffusing particles.

In the radio band, there are studies of the Crab Nebula since the early 1950s (see e.g. Mills 1952; Baars & Hartsuijker 1972; Duin & van der Laan 1972; Wilson 1972; Weiler 1975; Swinbank & Pooley 1979; Velusamy 1984; Velusamy et al. 1992, etc.) reporting total intensity and polarization measurements made at several frequencies with different instruments and various angular resolutions. Those early studies revealed an ellipsoidal source, somewhat larger than the optical remnant, with a filamentary appearance and a complex polarization structure. Bietenholz & Kronberg (1991) conducted VLA (NRAO) radio observations at 1.4 and 5 GHz, presenting polarization and Faraday rotation maps with the angular resolution of $1''.8$. Also, Bietenholz et al. (1991) used two-epoch high-resolution radio data to investigate the expansion of the outer edge of the nebula, finding that the expansion has accelerated since the supernova explosion. The center of the nebula and its dynamical changes were investigated in great detail in radio frequencies (Bietenholz et al. 2001, 2004), demonstrating that the radio wisps form elliptical ripples similar to the optical wisps in both morphology and behavior. However, from the comparison of radio to simultaneous optical images of the central part of the Crab Nebula, it is found that the radio wisps are sometimes displaced from the optical ones or have no optical counterparts, and the brightest optical wisps near the pulsar do not seem to have radio counterparts. On the contrary, in the exterior of the nebula there is a good general correspondence between the radio and optical features (Bietenholz et al. 2004).

In addition to the mentioned morphological characteristics, there can also be noted the “synchrotron bays,” large indentations on the periphery of the synchrotron nebula (one very clear to the east and the other somewhat less conspicuous to the west), a peculiarity that is evident in the optical continuum, UV, and IR images, but is less clear in radio and in X-ray (Wilson 1972; Seward 1989).

High linear polarization (between 30% and 60%) with radial orientation has been observed along the edges of the bays. The absence of synchrotron emission within the bays has been interpreted by invoking a magnetized torus encircling the remnant (probably formed by a disklike ejection from the progenitor star) that blocks the penetration of the relativistic particles from the pulsar creating these dark regions (Fesen et al. 1992).

As a part of a larger program dedicated to the investigation of the broad spectrum of the wisps and other central features near the pulsar, aiming at tracing the spectral energy distribution of the injected particles (Krassilchtchikov et al. 2014), we have undertaken a new detailed, almost contemporaneous, study of the Crab Nebula using the NRAO Karl Jansky Very Large Array (VLA)² at 3 GHz, the *Hubble Space Telescope* (*HST*) and *Chandra* telescopes. We have also used the Atacama Large Millimeter/submillimeter Array (ALMA) to produce the first detailed radio continuum image of the center of the nebula at 100 GHz, although the ALMA observations were not contemporaneous with the others. In this work we present the new 3 GHz radio image and first results of the ALMA 100 GHz observations, a new high spatial resolution UV image of the entire Crab Nebula obtained from data acquired by the Optical Monitor of *XMM-Newton* ($\lambda \sim 291$ nm), a new *HST* NIR image ($\lambda \sim 1.5\mu\text{m}$) and a new *Chandra* X-ray image in the 0.5–8.0 keV band. This paper is devoted to the detailed analysis of the morphological properties of the Crab Nebula across the electromagnetic spectrum. To carry out this comparison, in addition to our own new data we used existing *Spitzer* and *HST* images of the entire remnant kindly provided by T. Temim (data from Temim et al. 2006) and by A. Loll (data from Loll et al. 2013), respectively, which in spite of not being contemporaneous, are nevertheless useful for a comparative analysis of the larger scale structure.

2. OBSERVATIONS AND DATA REDUCTION

2.1. VLA radio data

² The Karl G. Jansky Very Large (EVLA) is operated by the National Radio Astronomy Observatory (NRAO), a facility of the National Science Foundation operated under cooperative agreement by Associated Universities, Inc.

Radio observations of the Crab Nebula were performed with the VLA of the NRAO on 2012 November 26 and 27 (Observing code VLA/12B-380, Legacy project AD670). The data set was acquired in the A-array configuration of the interferometer using the broadband VLA S-band receiver. The observations used two 1024 MHz independent basebands (covering a total bandwidth between 1988 and 3884 MHz) each with eight 128 MHz contiguous subbands, spread into 64 channels each. On both days we observed the source J0137+3309 (3C 48) as flux density and bandpass calibrator, setting the flux scale according to the coefficients derived at the EVLA by NRAO staff in 2010. Regular observations on the source J0559+2353 were used for phase calibration.

The raw visibilities were calibrated and imaged using the NRAO Common Astronomy Software Applications (CASA) package. Data from each day were first independently calibrated and then combined into a single uv data set to construct the final image. After initial data editing we determined the antenna gains across the bandwidth for flux and phase calibrators. Due to the presence of strong radio frequency interference, two spectral windows were dropped in both observing days. Before solving for the complex bandpass shape, we first estimated the relative delays of each antenna relative to the reference antenna. In the next step the calibration solutions were applied to the target source, which was then split out from the data set. We made the image using multi-frequency synthesis (MFS) and multi-scale (MS) CLEAN as implemented in CASA. This procedure accounts for variations in the synthesized beam while it solves for the scale size of the emission across the field of view. We set the Briggs robust parameter equal to 0.5, which represents a compromise between natural and uniform weighting. We then performed two rounds of self-calibration using the CLEAN models.

Observations in the A-array around 3 GHz provide information on spatial scales between the theoretical synthesized beam of $\sim 0''.7$ and the largest angular scale of $\sim 18''$ that can be well imaged at this frequency. This range allows us to map in high detail the thin radio wisps and synchrotron knots, but misses the extended features. To produce an image with the large-scale contributions, we followed a strategy somewhat similar to that described in [Bietenholz et al. \(2004\)](#) using the same 5 GHz image a template after correcting it for spectral differences in brightness to a frequency of 3

GHz and taking into account a long-term decay at a mean rate of 0.20 \% yr^{-1} (Aller & Reynolds 1985; Vinyaikin 2007). The resulting model was also spatially scaled to account for the nebular expansion at a rate of 0.13 \% yr^{-1} (Bietenholz & Nugent 2015). The CASA task FEATHER was used to combine the different spatial resolution images, using their Fourier transforms. The final 3 GHz image recovers a total flux density of 743 Jy and has a synthesized beam $0''.93 \times 0''.80$ at $\text{PA}=76^\circ.3$ and an rms noise level = $0.03 \text{ mJy beam}^{-1}$. The image produced with the contribution of all spatial scales recovered is presented in Figure 1.

Since the driving purpose of this work is to perform a detailed, comparative morphological analysis of the Crab Nebula across the electromagnetic spectrum, based on the same VLA data we produced another 3 GHz radio image using a lower weight factor for the contribution of the scaled lower resolution data. In essence this image is high-pass filtered, and some of the structure at larger spatial scales has been removed. At the cost of losing some smooth extended emission and not recovering the total flux density, the contrast is improved and all the thin structure, including narrow filaments and wisps, are better revealed. In the rest of the paper, we use this last image (shown in Figure 2) to match and analyze the small-scale structure.

2.2. ALMA radio data

To survey the central portion of the Crab Nebula at millimeter wavelengths, we used the ALMA 12 m array in the C32-4 configuration for a total of 2.2 hr and the ALMA compact array (ACA, A7 m) for a total of 6.6 hr in Band 3 (around 100 GHz, 3.3 mm) (Cycle 1, Program 2012.1.01099.S). The observations took place in blocks during several sessions between 2013-10-06 and 2014-05-04 (Cycles 1 and 2). The region observed was a rectangle $1'.5 \times 1'.1$ in size centered at $05^{\text{h}}34^{\text{m}}31^{\text{s}}$, $+22^\circ00'52''$ and tilted about 70° east of north. The area was surveyed through a mosaic of seven individual pointings separated by the Nyquist criterion. For the two arrays, 30 and 8 antennas were, respectively used. The sources J0423-1200, J0510+1800 and J0521+1638 were used for calibration. The correlator was configured to observe four 2000 MHz wide windows centered at 93, 95, 105, and 107 GHz, each divided in 128 channels spaced in 15.625 MHz.

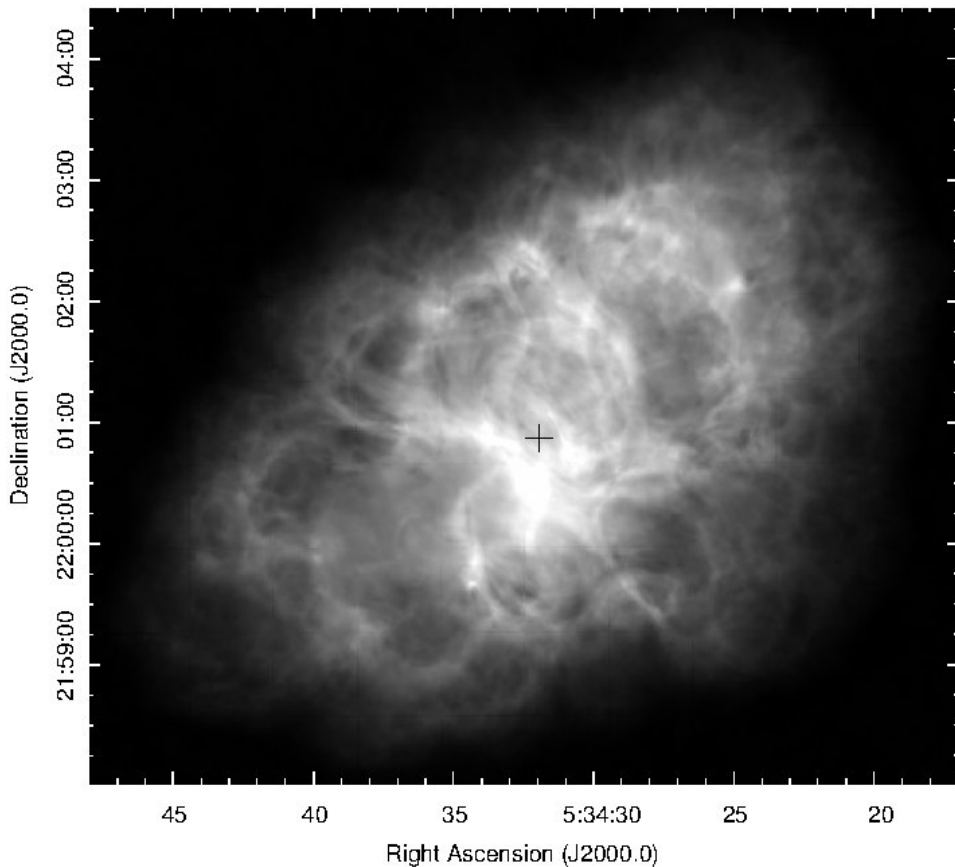


Figure 1. VLA radio image of the Crab Nebula at 3 GHz. It has $\text{HPBW} = 0''.93 \times 0''.80$ at $\text{PA}=76^\circ.3$ and a noise level of $0.03 \text{ mJy beam}^{-1}$. It is displayed in a linear scale between 0.09 and 17 mJy beam^{-1} . The plus sign shows the location of PSR B0531+21 (J0534+2200).

Automated pipeline processing was used to produce the images. The final image obtained with ACA 7 m array has $\text{HPBW} = 11''.9 \times 11''.6$, and for the 12 m array $\text{HPBW} = 1''.8 \times 1''.4$ and rms noise of $\sim 0.2 \text{ mJy beam}^{-1}$. The ACA observations were carried out to provide the missing short spacings contribution; however, the procedure was not completed because the 12 m array observations do not meet the quality expectations and the rms achieved was about 10 times worse than requested. The reason for that may be that in an effort to make this a short, fast project, a small mosaic covering only the central $\sim 5\%$ of the Crab Nebula was mapped. This area, although sufficient to match the contemporaneous *Chandra* and *HST* studies of the structures around the pulsar, turned out to be too small for a very bright radio source such as is the Crab Nebula, and much extended missing structure was left out, degrading the quality of the image. In addition, a problem that can result in small

distortions of the final image has been recently identified affecting mosaics observed during Cycles 1 and 2. But probably the main factor impeding the production of an optimal quality image is that the ALMA observations were not carried out within a small temporal window in coincidence with the VLA, *HST*, and *Chandra* campaigns (as originally requested by the authors) but spread over a six-month period. Therefore, in a target with rapidly moving features such as the wisps, which move with projected speeds of $\sim 0.2c$, the features moved about $3''$ (\sim two beams) over the time between consecutive observations, thus corrupting the image.

In spite of not achieving the expected quality, we report here the image obtained with the 12 m antennae array, where the central part of the Crab Nebula is shown for the first time at this high radio frequency with an arcsecond angular resolution. The main features are easily identified and can be used for visual morphological comparison. Because of the lack of short spatial frequencies in this image, there are negative values around the bright features. The new image presented here improves by a factor of 10 the angular resolution obtained at this frequency for the Crab Nebula up to the present (Arendt et al. 2011). The present observations will serve as a pathfinder for the optimally designed, deeper observations of the entire Crab Nebula with ALMA.

2.3. *HST* Near-IR Data

To accomplish the proposed morphological comparison across the electromagnetic spectrum, we produced a new high-angular resolution image of the Crab Nebula using the *HST*. Within a single *HST* orbit on 2012 November 26 (program ID 13043) we acquired four exposures with the WFC3/IR F160W filter (band: 1.4–1.7 μm) at four dither points using the WFC3-IR-DITHER-LINE pattern with the $0''.636$ spacing. This sequence uses evenly spaced 50 s time interval between nine reads. The images from the individual exposures were “drizzled” into a single image by the standard WFC3 pipeline processing. The total accumulated scientific exposure in the combined $123'' \times 136''$ image used in this paper is 1612 s. The PSF FWHM is $0''.15$.

2.4. *XMM-Newton* UV data

In the UV domain we produced a new image based on existing data using the broadband UVW1 filter centered at 291 nanometers (254 –328 nm at half maximum) of the Optical Monitor (OM) on board of *XMM-Newton*. The OM is a 30 cm diameter telescope that provides simultaneous observations in a $17' \times 17'$ field of view. The data were processed using the *XMM* Science Analysis Software (SAS).

Since the Crab Nebula is one of the main calibration sources for the *XMM-Newton* EPIC instrument, there is a good collection of images acquired with OM during the whole period that *XMM-Newton* has been operational. *XMM* SAS processing corrects every single image for the geometric distortion introduced by the OM detector. This allows us to align and co-add 75 images spanning 14 yr, between 2001 and 2015 with high accuracy, as it can be seen by looking at the stars in the field of view, which have an FWHM of $1''.7$ in the co-added image.

2.5. *Chandra* X-Ray Data

The Crab Nebula was observed with *Chandra* on 2012 November 26 (Obs. ID 14458). Due to the X-ray brightness of the Crab PWN, a single-chip graded³ ACIS-S observation (start time 56257.8736 MJD) was conducted with the shortest possible 0.2 s frame time for the 300×300 pixel spatial window. The dither amplitude was set to $1''$ to reduce the blurring. Due to the small frame time and telemetry saturation, the dead time was about 90% of the frame time, and the live time of the 10 ks exposure amounted to only 1244 s of useful scientific exposure. The resolution of the resulting 0.5-8 keV images is about $0''.4 - 0''.5$ (PSF FWHM), depending on the off-axis distance.

3. THE 3 GHZ AND 100 GHZ RADIO IMAGES

In Figure 2 we show the high-pass filtered (see Section 2) 3 GHz image of the Crab Nebula, which reveals the rich structure of the radio synchrotron emission. In addition to the well-known long, bright filaments, many short structures of different thickness and brightness are evident across the nebula. The resolved structure consists of a tangled net of intercrossed filaments that probably are

³ In the graded mode only the total reconstructed energy of an X-ray event is telemetered to the ground.

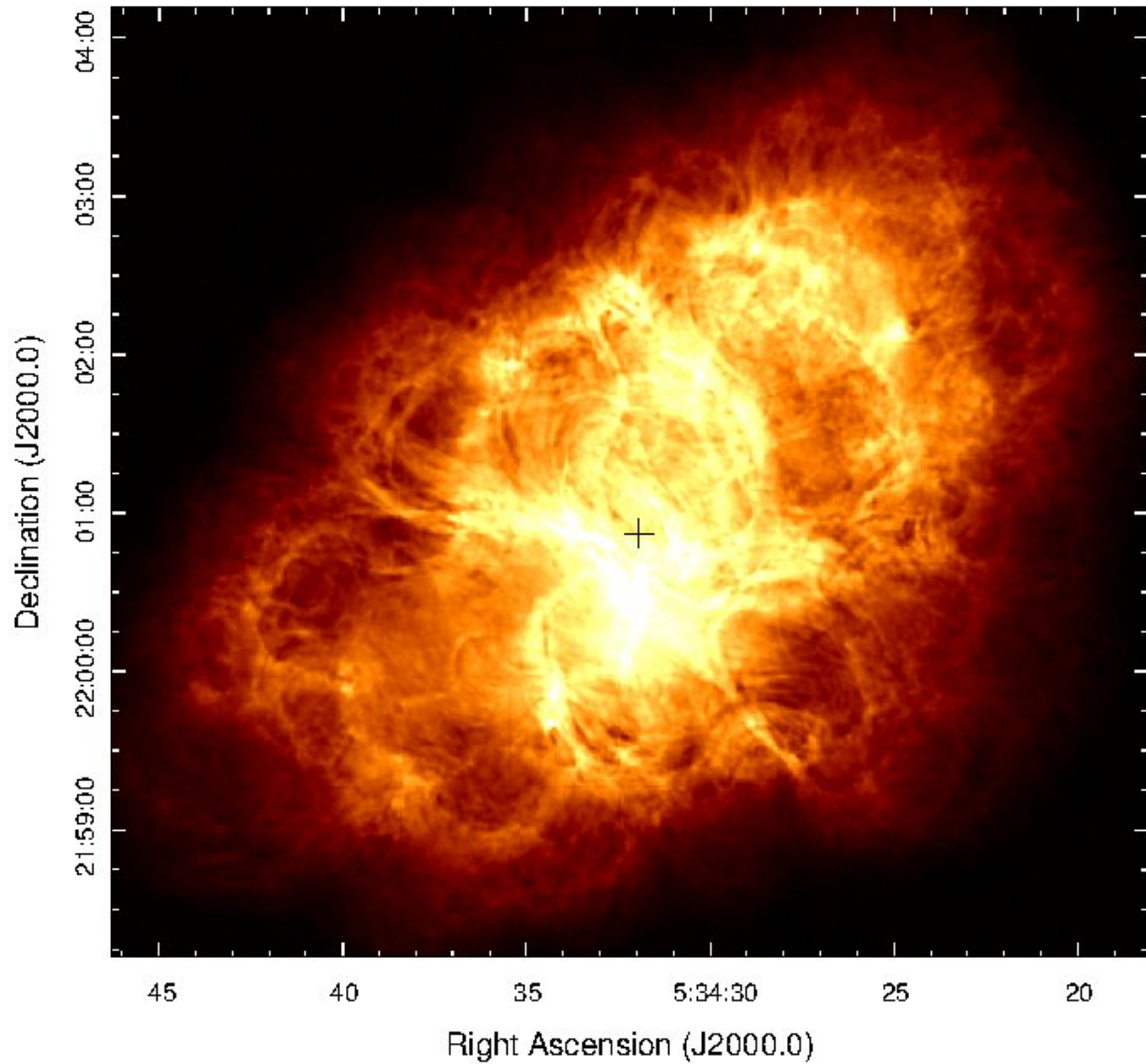


Figure 2. VLA radio image of the Crab Nebula at 3 GHz produced to improve the contrast and better reveal details of small-scale emission as described in Section 2. The beam is $0''.93 \times 0''.80$ at $PA=76^\circ 3$ and the rms noise level is $0.03 \text{ mJy beam}^{-1}$. It is displayed in a linear scale between 0.09 and $5.3 \text{ mJy beam}^{-1}$. The plus sign shows the location of the pulsar.

at different depths along the line of sight. Along the eastern and southern sides, the outer border of the nebula is clearly undulated, with large arches, as already noticed in the previous radio images of the Crab Nebula.

To analyze the structures in detail, in Figure 3 we show a close-up of the equatorial region of the Crab Nebula as seen at 3 GHz and at 100 GHz. The emission in this region consists of bright short filaments with different widths and orientations. Two long, almost parallel, bright filaments (more

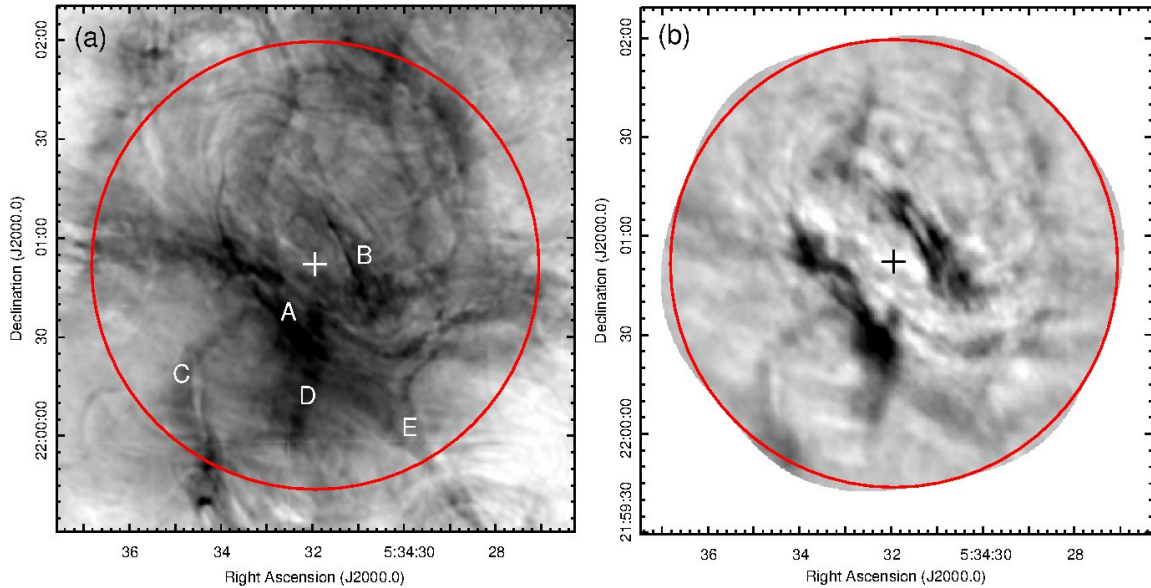


Figure 3. (a) VLA radio image of the central $\sim 2' \times 2'$ region of the Crab Nebula at 3 GHz. The gray scale varies between 1.4 and 5.8 mJy beam $^{-1}$. The image used is the spatially high-pass filtered as described in Section 2 to emphasize the fine structure. The features labeled A, B, C, D, and E are discussed in the text. (b) ALMA radio image at 100 GHz of the same area with HPBW = $1''.8 \times 1''.4$. The gray scale varies between -1.2 and 3.7 mJy beam $^{-1}$. Negative values are due to the lack of short spacing contributions in the image. A color-inverted display is used to emphasize the prominent features and the plus sign indicates the location of the pulsar in both panels.

evident in the image at 100 GHz) are noticed symmetrically located at each side of the pulsar (labeled as features A and B in Figure 3), at about $5''.5$ ($\sim 1.6 \times 10^{17}$ cm at 2 kpc) from the pulsar. Another conspicuous feature is the one named C in Figure 3, with a jet-like appearance, that will be discussed later. From the present radio observations, we can conclude that in the region around the pulsar the spatial distribution at 100 GHz is very similar in appearance to that observed at 3 GHz, although a firm conclusion will only be achieved based on an image at 100 GHz with all spatial scales recovered.

Other interesting features revealed by the 3 GHz observations are seen in Figure 4a, where we displayed a close-up of the eastern side of the nebula. It shows several peripheral arches (the loop-like features noticed by [Bietenholz & Kronberg 1991](#)) with small bright spots at their footpoints⁴ (to

⁴ The terminology to name these features is taken from the solar case because of their similar appearance.

guide the eye, we encircled the regions around the footpoints in Figure 4a). The arcs are composed of a series of narrow filaments, well resolved with the present observations, with widths of the order of $2''$ – $3''$ (~ 6 to 8×10^{17} cm at 2 kpc), that rise about $40''$ above the nebular region, while the separation between the bright spots at the base is of $\sim 66''$. Such topology resembles the complex system of arches observed in solar bursts, where the loops carry plasma confined to magnetic field lines, and the brightening at the footpoints results from particle acceleration and magnetic enhancement (see for example [Cristiani et al. 2008](#)). In the case of solar bursts it is found that the arches reconnect at low heights, and the reconnected arches are anchored in regions that have the magnetic field intensity about an order of magnitude higher than the field in the surroundings. The solar synchrotron radio emission comes from electrons spiraling down along the reconnected loops. Although the phenomena that give rise to the observed radio loops in the Crab Nebula have different scales than those acting at the solar bursts, the similarity in the morphology suggests that analogous magnetic loops may be present in the Crab PWN, with the caveat that the physical parameters (magnetic field strength, plasma density, etc.) of the respective environments are different by orders of magnitude. To have an idea, in the solar flares the magnetic fields at the footpoints are of the order of hundreds of Gauss and at the top around 10–50 Gauss ([Tandberg-Hanssen & Emslie 2009](#)), while in the Crab Nebula the magnetic field strength is of about 500 μ Gauss ([Hester et al. 1996](#)). Also the plasma density in solar flares is typically of the order of 10^9 to 10^{10} cm^{-3} ([Tandberg-Hanssen & Emslie 2009](#)), while in PWNe the ambient number density is of ~ 0.1 cm^{-3} ([Gaensler & Slane 2006](#); [Reynolds et al. 2012](#)).

In Figure 4b we focus on another peculiar feature, which is the set of loops with an arcade-like appearance⁵ (location marked by a white circle). This structure appears to be formed by closely packed arches wrapping around an almost straight bright filament (named E in Figure 3a). Such a topology can be produced if accelerated particles flowing from the pulsar along the filament carry a current, and the arcades are tracing the magnetic field lines wrapping around (assuming that the magnetic field lines are frozen into the plasma).

⁵ Again, we adopt solar terminology because of the strong resemblance in appearance. Solar arcades are a series of closely occurring loops of magnetic lines of force.

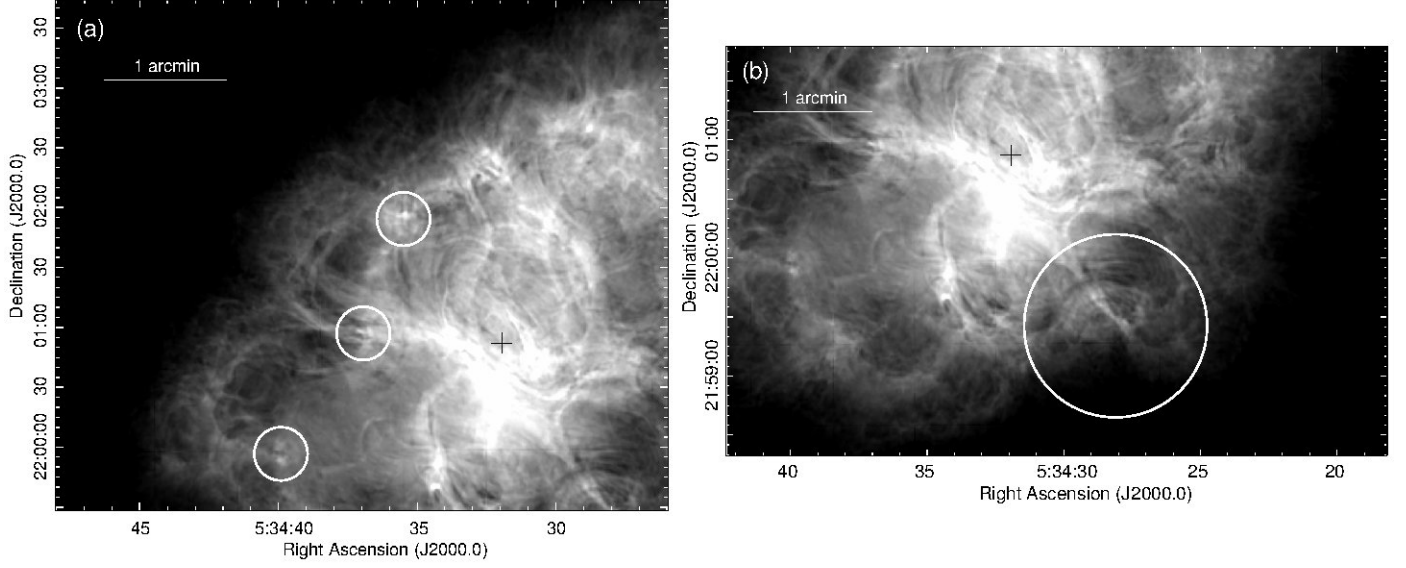


Figure 4. (a) Close-up view of the eastern flank of the Crab Nebula emphasizing the presence of arches and brightenings at the loop footpoints. The location of the footpoints are indicated by small white circles. (b) Close-up of the southwestern side. The circle marks the region where an arcade of loops is seen surrounding the filament labeled E in Figure 3a. For both figures the gray scale is linear and varies between 5 and 50 mJy beam^{-1} . The plus sign shows the location of the pulsar. The image used is the spatially high-pass filtered one to emphasize the fine structure (see Section 2).

In general, one can identify several sets of closely packed loops with different orientations across the nebula, except for the northwestern edge of the nebula, which looks more open than the rest. It should be noted that these loop-like features appear as a different component, distinct from the wisps and the extensive network of filaments that also shine in other spectral ranges, and that the Crab Nebula is unique among the PWNe observed in our Galaxy in displaying a morphology with loops at the periphery with such a clearness (see other PWNe morphologies for example in Gaensler & Slane 2006). Begelman (1998) suggested that kink instabilities can disrupt the concentric field structure in the nebula and drive the system toward a more chaotic structure that may form loops after reconnection. This hypothesis would be compatible with the widespread synchrotron loops and cellular structure of the magnetic field traced by the synchrotron emission.

In the following sections we analyze the possible correspondences between the radio emission and the radiation in other spectral ranges by comparing, for the first time, data with almost the same

angular resolution in all spectral ranges. Before combining all images were regridded to the same projection, coordinate frame, and geometry using AIPS tools. The co-alignment was done using the WCS tools in SAO DS9.

4. RADIO AND INFRARED

As summarized in Section 1 several studies of the Crab Nebula have been performed in the IR range. Here we have used the 3.6, 4.5, 5.8, 8.0, 24, and 70 μm images of the Crab Nebula obtained with the *Spitzer Space Telescope* IRAC and MIPS cameras (Temim et al. 2006) to compare with the radio emission distribution. At lower wavelengths (4.5 μm) the emission observed is mostly of synchrotron origin, while at higher wavelengths (8, 24, 70 μm), the emission is dominated by filaments of forbidden line emission (from S, Si, Ne, Ar, O, Fe, and Ni, Temim et al. 2012).

In Figure 5 we present a composite three-color image with radio emission in red, IR at 8 μm in green, and IR at 4.5 μm in blue. In this figure, all the prominent features around the pulsar (labeled from A to D in Figure 3(a)), are also bright in IR. The interior of the nebula is filled with synchrotron radiation, seen as bluish diffuse emission. The surrounding radio emission is traced in red. The IR synchrotron radiation seems to extend further toward the northwest than to the southeast, reaching in the northwest the same extension as the radio emission.

Another fact that can be seen from this comparison is related to the “bays”. As mentioned above, the east and west bays are two very conspicuous indentations located $\sim 80''$ east (around $5^{\text{h}}34^{\text{m}}37^{\text{s}}$, $+22^{\circ}00'57''$) and $\sim 75''$ west of the pulsar (around $5^{\text{h}}34^{\text{m}}26^{\text{s}}$, $+22^{\circ}00'35''$); pointed out by white arrows in Figure 5. These cavities were identified at the very discovery of the Crab Nebula in visible wavelengths, and later also detected in UV and IR. In radio, however, they are not obvious. In Figure 5, the superposition of IR and radio demonstrates that the radio emission follows the same concave morphology visible in IR, confirming that the bays are also traced in radio wavelengths, where they are somewhat hidden by the bright arched filaments. Particularly, in the case of the east bay, two sets of thin arched filaments seem to emanate from the center of the bay and curve toward the northwest and toward the southeast. It can be noticed that the bright footpoints around $5^{\text{h}}34^{\text{m}}36^{\text{s}}$, $+22^{\circ}01'00''$, mentioned earlier are also bright in IR. Along the boundary of the bays the

radio emission appears slightly exterior to the IR border, but this can be the consequence of the 10 yr lapse between the observations.

An additional characteristic from the IR-radio comparison that deserves to be mentioned is related to the structure that is displayed in Figure 4(b) and marked with a white circle in Figure 5. It can be noticed that the IR emission perfectly matches in shape and size the radio structure consisting of closely packed arches wrapping around the straight radio filament labeled E in Figure 3(a), which we called the “arcade” following the solar nomenclature. The same characteristic will be noticed again in Section 5 based on the comparison with the optical continuum emission.

5. RADIO AND OPTICAL

The comparison with the optical emission was carried out in two ways. First, for the complete nebula we used a set of images from the *HST* WFPC-2 survey carried out to cover the entire Crab Nebula (Loll et al. 2013). The survey includes eight WFPC-2 fields taken between 1999 October and 2002 January in the following filters: F502N ([OIII]), F673N ([SII]), F631N ([OI]), and F547M (a filter admitting a relatively line-free continuum). Second, to analyze the emission in the pulsar vicinity we used our own contemporaneous *HST* images described in Section 2. Although these observations lie in the near-IR range ($\lambda \sim 1.5\mu\text{m}$), we include them here for convenience.

In Figure 6(a) we present the comparison of distribution of the radio emission (in red) with the synchrotron-emitting optical continuum (in green) over the entire nebula. The optical synchrotron emission looks smoothly distributed and it appears to be completely confined within the radio nebula, as expected from the shorter lifetimes of the particles emitting in the visible range. Analogous to the IR synchrotron emission, the presence of the optical bays surrounded by radio emission with identical morphology can be noticed in Figure 6(a), again with a small shift owing to the time lapse between both observations. Another noticeable peculiarity is the distribution of the optical emission related to the “arcade” (shown in Figure 4(b) and Figure 5). The region is zoomed in Figure 6(b) to display the structure in detail. As already noticed in the previous section, it is remarkable how the synchrotron emission, in the optical range in this case, exactly reproduces the radio arcade-like morphology around the straight filament labeled E.

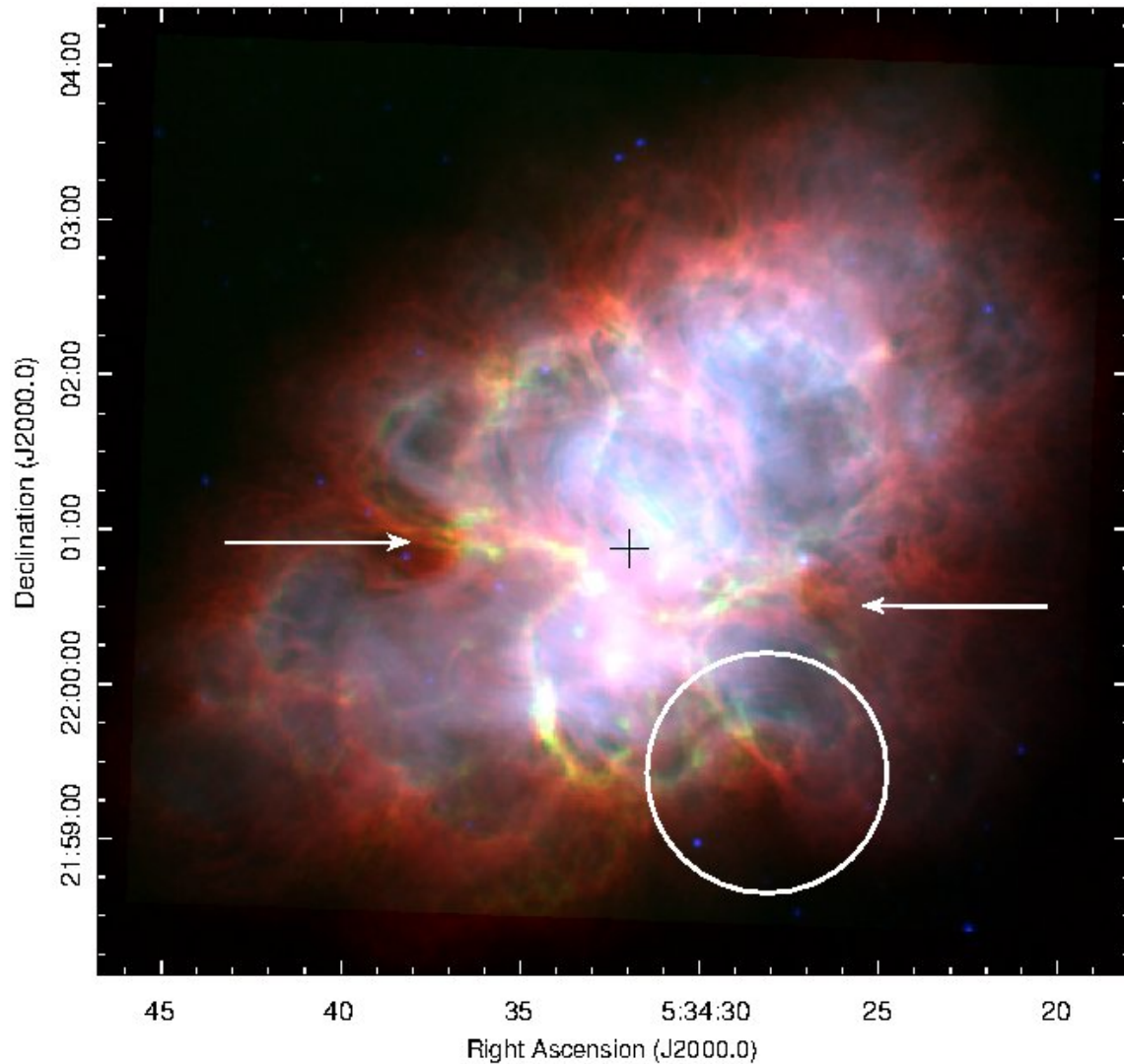


Figure 5. Comparison of the radio nebula (in red) with the *Spitzer* image at $\lambda 8 \mu\text{m}$ (in green) and in $4.5 \mu\text{m}$ (in blue). The white arrows point out the eastern and western “bays” discussed in the text. The white circle marks the same region as in Figure 4b, where an arcade of loops surrounds filament E. The radio image used is the spatially high-pass filtered to emphasize the fine structure (see Section 2). The plus sign shows the location of the pulsar.

Figure 6(c) displays in two colors a composition of the radio emission (in red) and the high-ionization [OIII] filamentary structure (in blue). The high-ionization emission lines trace the interface between the synchrotron nebula and the ejecta and are part of what Hester et al. (1996) named the “skin,” consisting of swept-up thermal ejecta that are being accelerated by the pressure of the synchrotron plasma (Hester et al. 1996; Sankrit et al. 1998; Hester 2008). As noticed before, the optical emission

lines define the outer edge of the Nebula around most of its periphery except for the northwestern portion (Loll et al. 2013). From the present comparison carried out with a very sensitive radio image, we confirm that the optical radiative shock at the boundary defines the outermost border of the Crab Nebula (Hester 2008, and references therein).

For the region around the pulsar, where small-scale features are highly variable, we performed the multiwavelength comparison using the *HST* data acquired on the same day as the radio one (about 11 hr later). In Figure 7(a) we present the *HST* WFC3/NIR image at $1.5\mu\text{m}$. The well-known narrow wisps are more prominent to the northwest of the pulsar, tracing concentric ellipses around the pulsar. Also, a few narrow filaments of different extensions (indicated in the figure) can be seen running from the central plane to the north. As it will be shown below, these filaments have clear radio counterparts. In the southern half the most conspicuous features are two broad structures, the one to the east being the optical counterpart of the pulsar jet, and the one to the west the counterpart of the feature labeled D in the radio image (Figure 3(a)). It can be noticed that none of them have their starting point at the pulsar. The pulsar jet is visible approximately from the inner elliptical ring, while feature D seems to originate at a site about $12''$ south (see also Figure 10).

In Figure 7(b) we present the superposition of the radio nebula (in magenta) with the same NIR image (in green). The regions where both emissions overlap are white. Although, as already noted, there is no a close correspondence of features, some agreement can be noticed in the region adjacent to the pulsar. In the first place, the distribution of the radio wisps follows quite accurately the elliptical shape as traced by the NIR emission, although they do not overlap. In the inner ring, to the northwest of the pulsar, the radio wisps appear to shine in between NIR wisps. The denoted “filaments” in Figure 7(a) and (b), are conspicuous in both spectral ranges. To the south, we can notice that the radio-jet-like feature labeled C (Figure 3(a)) does not have an NIR counterpart (it is only seen in magenta color), while the pulsar jet (which is also bright in X-rays) does not have a radio counterpart (only seen in green color). Feature D appears emitting both in radio and NIR. These last three structures will be considered again in the context of the X-ray emission analysis.

6. RADIO AND ULTRAVIOLET

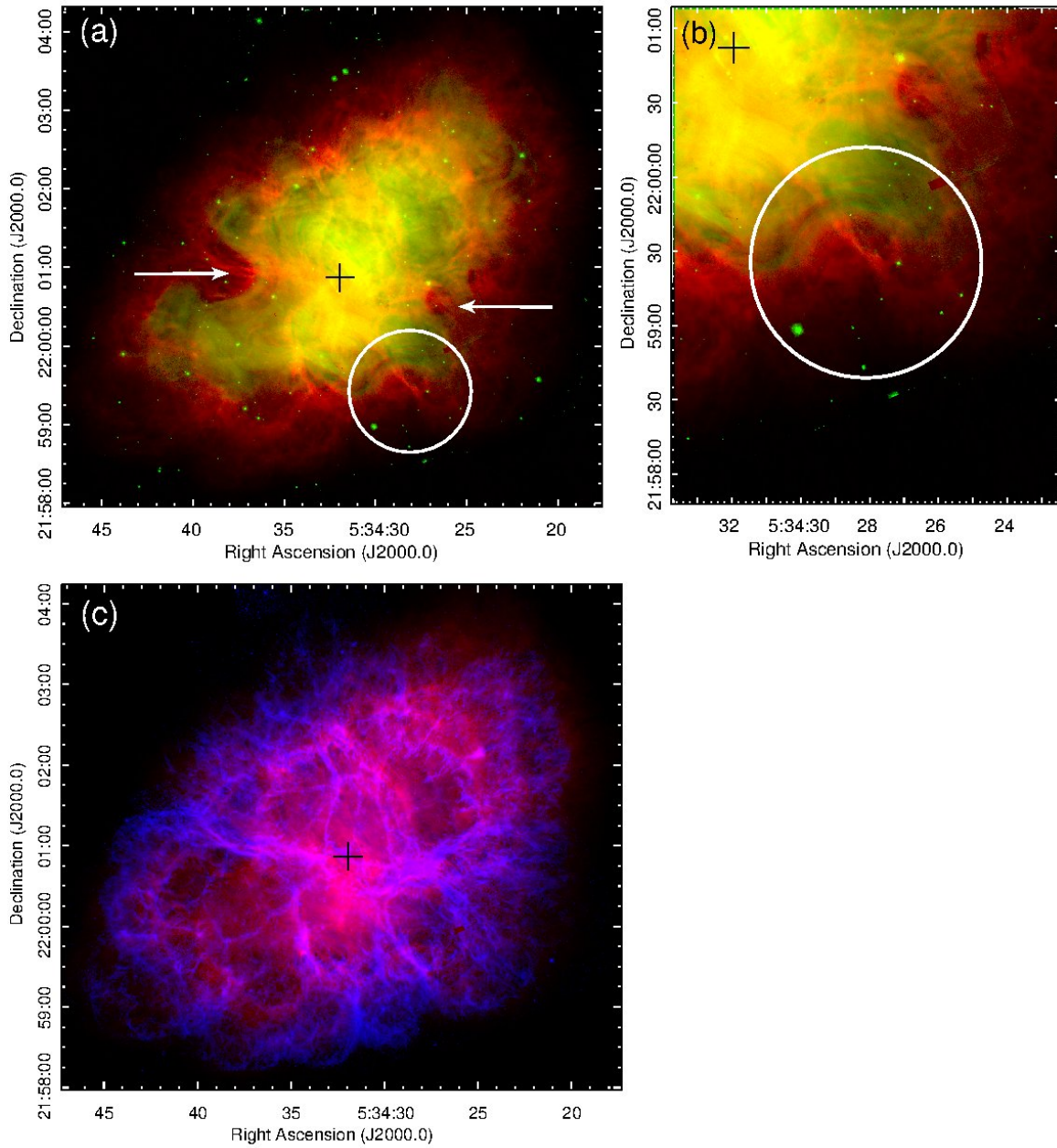


Figure 6. (a) Composition of radio emission at 3 GHz (in red, displayed with a linear scale between 0.05 and 5.3 mJy beam⁻¹) with the optical continuum (in green) as observed in the filter F547M. The white arrows point out the eastern and western “bays” discussed in the text. The white circle marks the “arcade” region. (b) Zoom around the “arcade-like” structure. (c) Comparison of the radio emission at 3 GHz (in red) with the [OIII] λ 5007 image (in blue). This combination highlights the fact that the radio synchrotron nebula is bounded by the region with high-ionization optical emission lines. The plus sign shows the location of the pulsar. The radio image used is the spatially high-pass filtered one to emphasize the fine structure (see Section 2).

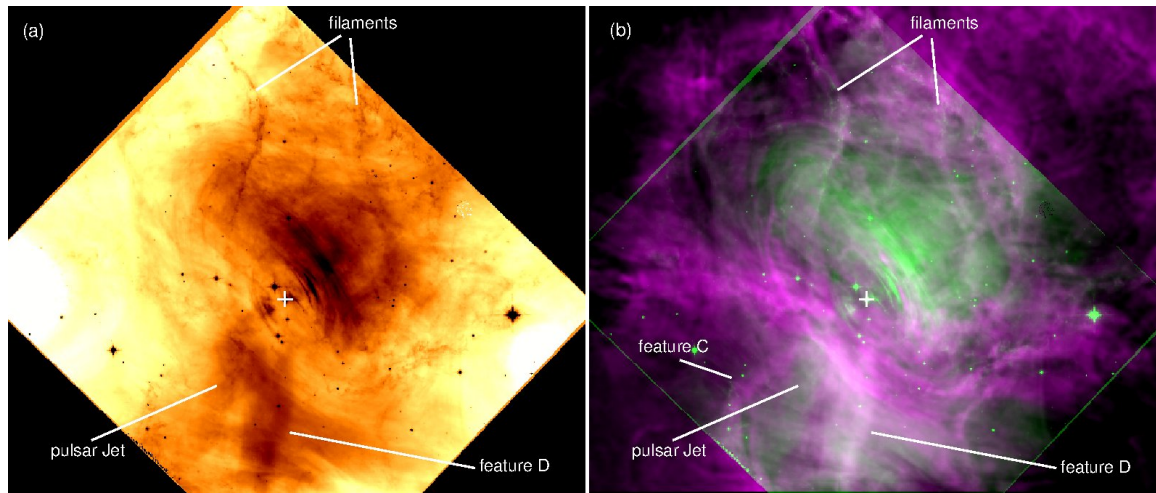


Figure 7. (a) *HST* WFC3/NIR image at $1.5\mu\text{m}$ of the central region of the Crab Nebula. (b) Comparison of the radio emission at 3 GHz (in magenta) with *HST* near-IR emission. The plus sign shows the location of the pulsar. Labeled features are discussed in the text. The radio image used is the spatially high-pass filtered one to emphasize the fine structure (see Section 2).

Not many studies in the UV of the Crab Nebula have been published to date (e.g. Davidson et al. 1982; Blair et al. 1992; Hennessy et al. 1992; Sollerman et al. 2000), and they were mainly dedicated to spectroscopy of the brightest filamentary structure and/or selected regions. In a UV band comparable to the present data, it can be mentioned that Hennessy et al. (1992) obtained images of the entire nebula in UV at 150, 160, and 250 nm by using the Ultraviolet Imaging Telescope in the Astro-1 Shuttle, with FWHM of $\sim 5''$, $\sim 3''.6$ and $\sim 4''$, respectively. Figure 8(a) shows a new image of the Crab Nebula in UV wavelengths around 291 nm, obtained with an FWHM of $1''.7$.

From Figure 8 we see that the equatorial features are brighter northward of the pulsar, as in the rest of investigated wavelengths. Only hints of the southern jet can be traced, somewhat confused with more diffuse emission⁶. The eastern and western bays are very conspicuous features in the UV. With the appropriate contrast it can be noticed that the UV radiation covers an area almost as extensive as the radio nebula. In Figure 8(b) we present a two-color image combining radio emission (in red) with the UV (in green). In particular, radio and UV emissions overlap in features A, B,

⁶ If the UV jet moves around as the X-ray jets does, then the image may be blurred because of averaging over a large time interval

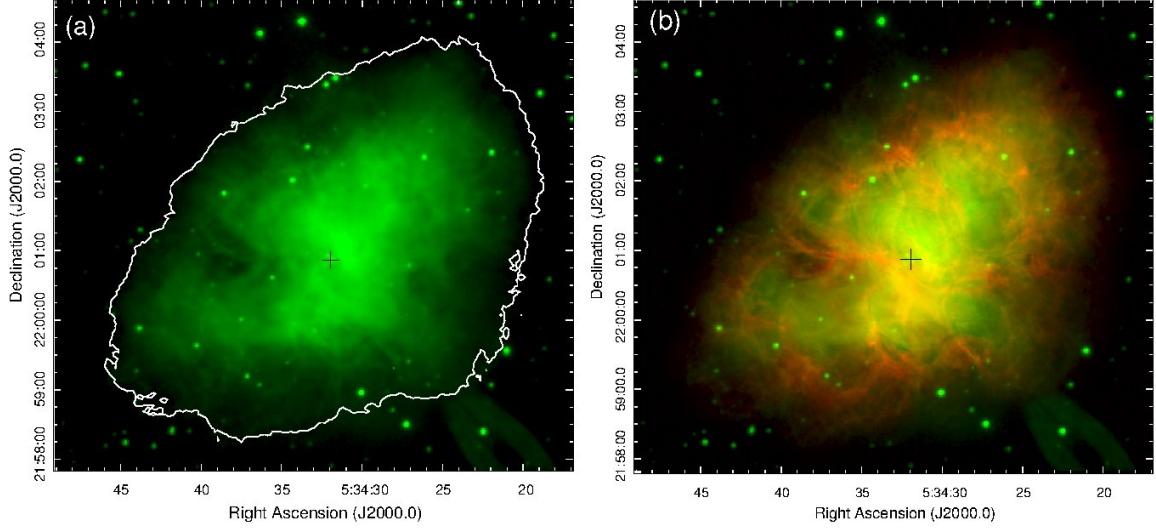


Figure 8. (a) Crab Nebula as observed in UV (around 291 nm) by the Optical Monitor on board *XMM-Newton*. To illustrate the extension of the UV emission, a radio contour traced at $0.4 \text{ mJy beam}^{-1}$ is plotted. (b) Comparison of 3 GHz radio nebula (in red) with the UV emission (in green). The plus sign shows the location of the pulsar. The radio image used is the spatially high-pass filtered one to emphasize the fine structure (see Section 2).

D, and E, in the equatorial region. Based on the extension and great morphological similitude with the continuum optical and infrared emission, we suggest that the UV emission shown in Figure 8 is probably of synchrotron origin.

7. RADIO AND X-RAYS

Figure 9(a) shows the X-ray image of the central region of the Crab Nebula as obtained during the 2012 *Chandra* campaign. It shows the knotty bright inner ring (the “inner ring” described by Weisskopf et al. 2012), the elliptical torus with bright wisps, and the jet extending to the southeast. The southeastern jet extends about $17''$ in a more or less straight way along the spin axis direction from the inner ring up to the position $\sim 5^{\text{h}}34^{\text{m}}33^{\text{s}}, +22^{\circ}00'40''$, where it bends to the south extending for $\sim 31''$, and ends in a curl, near $5^{\text{h}}34.5^{\text{m}}33^{\text{s}}, +22^{\circ}00'10''$. The jet appears well collimated only in the first section, and then it gets progressively fainter and broader with distance. Multiyear *Chandra* observations show that the X-ray jet changes its shape (Weisskopf et al. 2012), which could

be explained by either precession of the curved jet or by the motion of kinks along it (Kargaltsev et al. 2015, and references therein).

To compare in detail the X-ray radiation with the radio emission, we present in Figure 9(b) the superposition of the present *Chandra* X-ray image with the VLA 3 GHz image. The most striking feature of this figure is the presence of two separate jet-like features, one emitting in X-rays (in green) and the other in radio⁷ (in red), corresponding to the feature labeled C (Figure 3(a)). From the comparison of the new 3 GHz radio image with that at 5 GHz obtained in 2001 and reported by Bietenholz et al. (2004), we conclude that the “radio-jet” did not change along the 11 yr time span, neither in shape nor in position.

The X-ray jet and the “radio-jet” do not start at the same distance from the pulsar. While the X-ray jet appears to have its starting point at the innermost ring around the pulsar, the “radio-jet” starts at a larger distance from the pulsar, near the radio feature that we identified as “A” in Figure 3(a). Sky projections of the radio and X-ray jet-like features cross at the point where the X-ray emission makes the curl. After that point the radio emission broadens and bends to the south, extending for about 43'' where it ends in a small, bright knot at $5^{\text{h}}34^{\text{m}}34^{\text{s}}, +21^{\circ}59'40''$. The two jet-like features could be unrelated structures whose projections overlap in the plane of the sky. Alternatively, both the X-ray and radio jets might be due to synchrotron emission of relativistic particles supplied by the pulsar. In this case we should understand why the radio-emitting particles follow a different path than the X-ray-emitting particles.

8. SIMULTANEOUS VIEW OF THE VENTRAL PWN IN THREE SPECTRAL BANDS

For a quick view of similarities and differences in the appearance of the central PWN, in Figure 10 we show the three 2012 November 26 images (from left to right: the central region of the Crab Nebula is shown in radio, near-IR, and X-rays). To help the comparison we have overplotted the coordinates grid, an outer ellipse that approximately depicts the toroidal structure around the pulsar, and an

⁷ The presence of this structure was previously communicated by Kargaltsev et al. (2015) based on the same VLA image presented here.

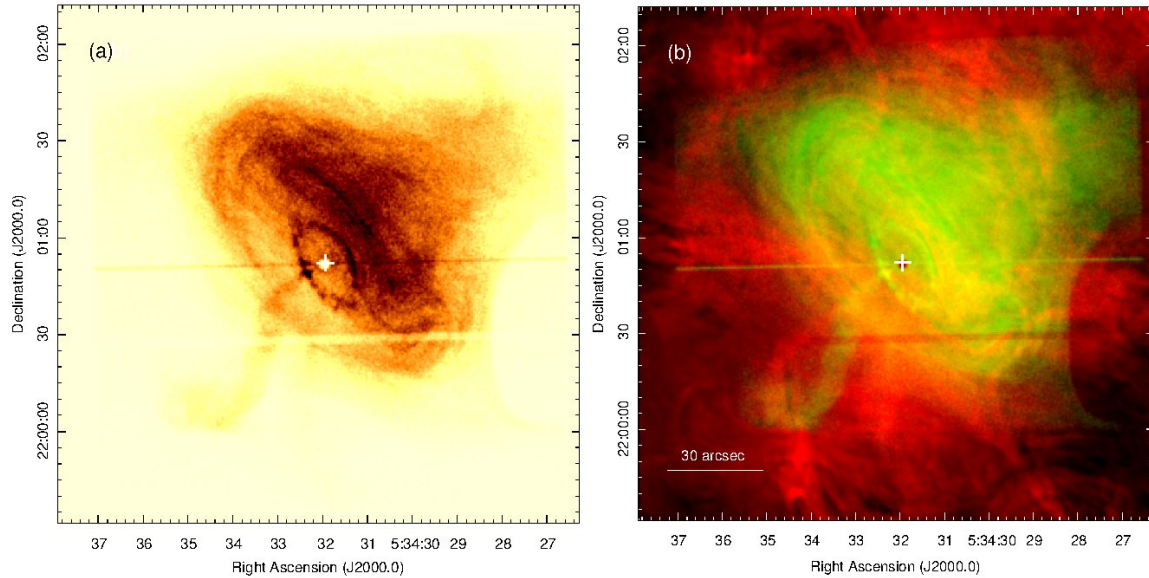


Figure 9. (a) *Chandra* X-ray image in the 0.5-8 keV band as obtained in the 2012 campaign. (b) The same X-ray image (in green) overlapping the 3 GHz radio emission (in red). The plus sign shows the location of the pulsar in both images. The radio image used is the spatially high-pass filtered one described in Section 2 to emphasize the fine structure.

internal ellipse coincident with the inner X-ray knotty ring. This figure confirms that even the bright wisps located northwest of the pulsar (the only features around the pulsar that have the same shape in the different spectral ranges) do not match in any of the images shown, the greatest differences being found with the radio emission. Also, from Figure 10, it is readily apparent that while in the radio band the brightest features are preferentially located southeast of the pulsar, at higher energies the northwestern side is more prominent.

To explain the lack of spatial coincidence between radio features and the radiation in the optical and X-rays ranges in the pulsar torus, [Komissarov \(2013\)](#) proposed that the radio wisps could just be some kind of ripples driven by the unsteady outflow from the termination shock through the PWN. In this case, there should be delayed changes in the radio wisp positions, which would correlate with the changes in the X-ray ring shape/brightness. To look for these correlations one needs to carry out radio follow-up of X-ray monitoring observations on longer timescales. An alternative explanation, also suggested by [Komissarov \(2013\)](#), is that the radio particles come from different parts of the termination shock. The existence of two synchrotron components of different origin was earlier

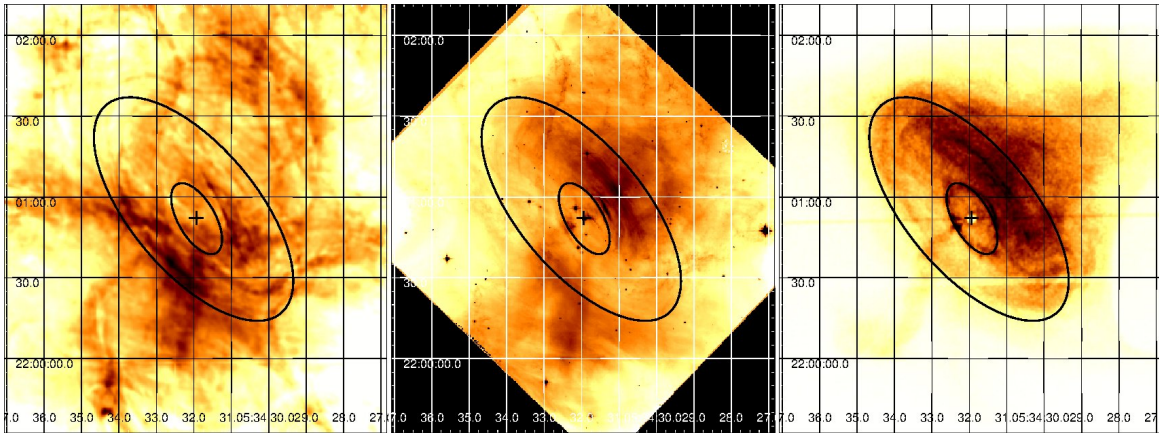


Figure 10. From left to right: radio, NIR, and X-ray contemporaneous images of the center of the Crab Nebula. An inverted color scheme is used to improve the display of features (darker is brighter). The plus sign shows the location of the pulsar. The radio image used is the spatially high-pass filtered one (see Section 2) to emphasize the fine structure. The overplotted ellipses are discussed in the text.

proposed by [Bandiera et al. \(2002\)](#) to explain spectral peculiarities between the radio emission at 20 cm and at 1.3 mm. Also, [Schweizer et al. \(2013\)](#) proposed that the X-ray and the optical emission must be produced by different populations of particles. Further investigations are required to discern the origin and distribution of the synchrotron radiation in the different spectral ranges.

9. SUMMARY

We have presented a completely new set of images of the Crab Nebula, from radio to X-rays, including a VLA radio image at 3 GHz with subarcsecond angular resolution (entire nebula), the first ALMA image at 100 GHz (central region), an *HST* WFPC3 F160W NIR image (central region), an *XMM-OM* UV image around 291 nm (entire nebula), and a *Chandra* ACIS X-ray image (central region). Based on these images and previous *Spitzer* IR and *HST* optical images of the Crab Nebula, we carried out a detailed analysis of the morphological properties of the nebula across the electromagnetic spectrum, with particular emphasis on the central region where we compared almost simultaneous images.

Our main findings are as follows:

1. The radio emission at 3 GHz shows the well-known undulated border. Particularly, toward the east, southeast, and south, well-defined arches composed of a series of narrow filaments dominate

the edge appearance. Along the eastern boundary these filaments form large curved features with footpoint brightenings that we interpret as produced by particle acceleration and magnetic enhancement, in an analogy with solar phenomena that produce a similar topology. Also, in the southwest part of the nebula a set of closely packed arches can be observed wrapping around a long filament that comes from the equatorial region, with a morphology resembling the solar “arcades” formed by closely occurring loops of magnetic lines of force. We suggest that the loop-like structures originate in plasma confined to magnetic field lines, and the magnetic fields are restructured by plasma kink instabilities, which change the magnetic structure from the central toroidal geometry with nested loops, into a chaotic structure with loops throughout the nebula, as proposed by [Begelman \(1998\)](#).

2. A preliminary look at the central region of the nebula as observed for the first time at 100 GHz with angular resolution better than $2''$, suggests that the radio synchrotron emission has the same spatial distribution up to millimeter wavelengths, a frequency where the emitting electrons are over five times more energetic than those emitting at 3 GHz. More observations of the entire nebula are required to confirm the results.

3. The continuum synchrotron emission of the Crab Nebula as mapped with *Spitzer* in IR, in optical with the *HST*, and in the new *XMM-OM* UV image, shows two very conspicuous “bays,” one to the east and one to the west. They are peripheral indentations of the Crab Nebula probably produced by a pre-supernova disklike magnetized torus that blocks the penetration of relativistic particles. From the present comparison with the radio image, it is possible to confirm that the bays are also a morphological property of the radio emission (the east bay being better defined). The richness of the borderline features masks these indentations in the radio regime. Also, the present multiwavelength comparison revealed that the “arcade-like” feature observed in radio is clearly detected in IR (at $4.5 \mu\text{m}$ that traces the synchrotron component) and in the optical continuum.

4. The comparison of the high-dynamic range 3 GHz image with the *HST* mosaic obtained in the [OIII] line (from [Loll et al. 2013](#)), confirms that the swept-up thermal ejecta accelerated by the pressure of the PWN plasma traces the outer edge of the Nebula around most of its periphery, with the only exception for the northwestern portion.

5. The new *HST* NIR image of the central region shows the well-known elliptical torus around the pulsar, composed of a series of concentric narrow features of variable intensity and width. The emission is in general more prominent northwest of the pulsar.

6. The comparison of the radio and the X-ray emission distributions in the central region suggests the existence of a double-jet system from the pulsar, one detected in X-rays and the other in radio. None of them starts at the pulsar itself but in its environs. The X-ray jet begins at the bright inner ring, while what we call the “radio-jet” appears to start in a radio feature located about $5''.5$ ($\sim 1.6 \times 10^{17}$ cm at a distance of 2 kpc) southeast from the pulsar. Contrary to the X-ray jet whose shape changes with time, from the comparison of the new 3 GHz image with previous radio images we conclude that the “radio-jet” looks constant in shape and position along the years.

7. The comparison of simultaneous multiwavelength emission in the vicinity of the pulsar suggests the existence of at least two different synchrotron components.

G.D. and G.C. are members of the *Carrera del Investigador Científico* of CONICET, Argentina. We thank C. Mandrini for the useful discussions about solar phenomena. This work was partially supported by grants awarded by CONICET (PIP 0736/11) and ANPCYT (PICT 0571/11), Argentina. O.K. acknowledges partial support from the Chandra Award GO3-14084X issued by the Chandra X-ray Observatory Center, and Hubble Space Telescope award HST-GO-13043.009-A issued by the Space Telescope Science Institute. This paper makes use of the following ALMA data: ADS/JAO.ALMA#2012.1.01099.S. ALMA is a partnership of ESO (representing its member states), NSF (USA) and NINS (Japan), together with NRC (Canada) and NSC and ASIAA (Taiwan), in cooperation with the Republic of Chile. The Joint ALMA Observatory is operated by ESO, AUI/NRAO and NAOJ. This research has made use of SAOImage DS9, developed by Smithsonian Astrophysical Observatory.

REFERENCES

Aller, H. D., & Reynolds, S. P. 1985, *ApJL*, 293,
L73

Arendt, R. G., George, J. V., Staguhn, J. G.,
et al. 2011, *ApJ*, 734, 54

- Baars, J. W. M., & Hartsuijker, A. P. 1972, *A&A*, 17, 172
- Bandiera, R., Neri, R., & Cesaroni, R. 2002, *A&A*, 386, 1044
- Begelman, M. C. 1998, *ApJ*, 493, 291
- Bietenholz, M. F., Frail, D. A., & Hester, J. J. 2001, *ApJ*, 560, 254
- Bietenholz, M. F., Hester, J. J., Frail, D. A., & Bartel, N. 2004, *ApJ*, 615, 794
- Bietenholz, M. F., & Kronberg, P. P. 1991, *ApJ*, 368, 231
- Bietenholz, M. F., Kronberg, P. P., Hogg, D. E., & Wilson, A. S. 1991, *ApJL*, 373, L59
- Bietenholz, M. F., & Nugent, R. L. 2015, *MNRAS*, 454, 2416
- Blair, W. P., Long, K. S., Vancura, O., et al. 1992, *ApJ*, 399, 611
- Bowyer, S., Byram, E. T., Chubb, T. A., & Friedman, H. 1964, *Science*, 146, 912
- Brinkmann, W., Aschenbach, B., & Langmeier, A. 1985, *Nature*, 313, 662
- Bühler, R., & Blandford, R. 2014, *Reports on Progress in Physics*, 77, 066901
- Cristiani, G., Giménez de Castro, C. G., Mandrini, C. H., et al. 2008, *A&A*, 492, 215
- Davidson, K., Gull, T. R., Maran, S. P., et al. 1982, *ApJ*, 253, 696
- Douvion, T., Lagage, P. O., Cesarsky, C. J., & Dwek, E. 2001, *A&A*, 373, 281
- Duin, R. M., & van der Laan, H. 1972, *Astrophys. Lett.*, 12, 177
- Fesen, R. A., Martin, C. L., & Shull, J. M. 1992, *ApJ*, 399, 599
- Gaensler, B. M., & Slane, P. O. 2006, *ARA&A*, 44, 17
- Gomez, H. L., Krause, O., Barlow, M. J., et al. 2012, *ApJ*, 760, 96
- Green, D. A., Tuffs, R. J., & Popescu, C. C. 2004, *MNRAS*, 355, 1315
- Gursky, H., Giacconi, R., Paolini, F. R., & Rossi, B. B. 1963, *Physical Review Letters*, 11, 530
- Hennessy, G. S., O'Connell, R. W., Cheng, K. P., et al. 1992, *ApJL*, 395, L13
- Hester, J. J. 2008, *ARA&A*, 46, 127
- Hester, J. J., Scowen, P. A., Sankrit, R., et al. 1995, *ApJ*, 448, 240
- Hester, J. J., Stone, J. M., Scowen, P. A., et al. 1996, *ApJ*, 456, 225
- Kargaltsev, O., Cerutti, B., Lyubarsky, Y., & Striani, E. 2015, *SSRv*, 191, 391
- Komissarov, S. S. 2013, *MNRAS*, 428, 2459
- Krassilchtchikov, A., Bykov, A., Kargaltsev, O., et al. 2014, in *COSPAR Meeting*, Vol. 40, 40th COSPAR Scientific Assembly
- Loll, A. M., Desch, S. J., Scowen, P. A., & Foy, J. P. 2013, *ApJ*, 765, 152
- Madsen, K. K., Reynolds, S., Harrison, F., et al. 2015, *ApJ*, 801, 66
- Marsden, P. L., Gillett, F. C., Jennings, R. E., et al. 1984, *ApJL*, 278, L29
- Mills, B. Y. 1952, *Nature*, 170, 1063
- Mori, K., Burrows, D. N., Hester, J. J., et al. 2004, *ApJ*, 609, 186

- Persi, P. 2012, *Mem. Soc. Astron. Italiana*, 83, 92
- Reynolds, S. P., Gaensler, B. M., & Bocchino, F. 2012, *SSRv*, 166, 231
- Sankrit, R., & Hester, J. J. 1997, *ApJ*, 491, 796
- Sankrit, R., Hester, J. J., Scowen, P. A., et al. 1998, *ApJ*, 504, 344
- Schweizer, T., Bucciantini, N., Idec, W., et al. 2013, *MNRAS*, 433, 3325
- Seward, F. D. 1989, *SSRv*, 49, 385
- Seward, F. D., Tucker, W. H., & Fesen, R. A. 2006, *ApJ*, 652, 1277
- Sollerman, J. 2003, *A&A*, 406, 639
- Sollerman, J., Lundqvist, P., Lindler, D., et al. 2000, *ApJ*, 537, 861
- Swinbank, E., & Pooley, G. 1979, *MNRAS*, 186, 775
- Tandberg-Hanssen, E., & Emslie, A. G. 2009, *The Physics of Solar Flares*
- Temim, T., & Dwek, E. 2013, *ApJ*, 774, 8
- Temim, T., Sonneborn, G., Dwek, E., et al. 2012, *ApJ*, 753, 72
- Temim, T., Gehrz, R. D., Woodward, C. E., et al. 2006, *AJ*, 132, 1610
- Trimble, V. 1973, *PASP*, 85, 579
- Tziamtzis, A., Lundqvist, P., & Djupvik, A. A. 2009, *A&A*, 508, 221
- Velusamy, T. 1984, *Nature*, 308, 251
- Velusamy, T., Roshi, D., & Venugopal, V. R. 1992, *MNRAS*, 255, 210
- Vinyaikin, E. N. 2007, *Astronomy Reports*, 51, 570
- Weiler, K. W. 1975, *Nature*, 253, 24
- Weisskopf, M. C., Elsner, R. F., Kolodziejczak, J. J., O'Dell, S. L., & Tennant, A. F. 2012, *ApJ*, 746, 41
- Weisskopf, M. C., Hester, J. J., Tennant, A. F., et al. 2000, *ApJL*, 536, L81
- Wilson, A. S. 1972, *MNRAS*, 157, 229